Detrimental Effect Elimination of Current Sensor Accuracy Uncertainty for High-Precision Position Sensorless Control of IPMSM Drives

Jiadong Lu, *Member, IEEE*, Yihua Hu, Senior *Member, IEEE,* Jinglin Liu, *Member, IEEE,* Kai Ni, *Student Member, IEEE,* and Huiqing Wen, Senior *Member, IEEE*

***Abstract*—The precision of position estimation is highly dependent on the accuracy of multiple current sensors. Whereas the conventional error calibration strategies for current sensor accuracy uncertainty (SAU) problem have limitations regarding the position sensorless controlled drives. In order to solve this thorny problem, this paper proposes a mutual calibration strategy for the multiple current sensors in an IPMSM drive. The proposed current sensor error calibration strategy takes full advantage of the correlation among the multiple current sensors themselves without using any complicated observers. Moreover, the traditional seven-segment space vector pulse-width modulation (SVPWM) technology is applied without modification. The only change is reflected in several sets of the artificially added current sampling points. The effectiveness of the proposed strategy is verified by experimental results on a 5kW IPMSM motor prototype, which shows that the calibrated current sensors exhibit improved accuracy, and the position estimation accuracy is also guaranteed.**

***Index Terms*—Current sampling error, estimation error, interior permanent magnet synchronous motor (IPMSM), mutual calibration, position sensorless control.**

I. Introduction

INTERIOR permanent magnet synchronous motor (IPMSM) is a promising motor for industrial and household applications due to its outstanding features compared with other kind of motors [1]-[5]. A vector controlled IPMSM drive usually consists of one position and several current sensors [6], [7]. High accuracy and healthy conditions of these crucial sensors are of great significance to the normal operation of the drive [8]. Encoder, known as a widely used type of position sensor for IPMSM drives, requires additional volume, installation and cost for its application, which also suffers from faults [9]. Therefore, during the last few decades, many research efforts were devoted to achieving high performance for motor drives without employing encoders [10]-[14]. Among all these methods, sensorless control is the one that attracts much attention thanks to its fine feasibility and high estimation accuracy [15]-[21]. It is usually realized by using the current signals on the motor windings to estimate the rotor position information, which utilizes the characteristics of motor saliency or mathematical model. Therefore, in a manner of speaking, the accuracy of multiple current sensors determines the position estimation precision of sensorless estimation [22]. In [22], the author pointed out that the current measurement errors are the main source that causes the estimation error for stator model based flux estimator.

Usually a sensorless IPMSM drive contains two phase and one DC-bus current sensors. The accuracy degradation of these crucial sensors due to temperature drift, aging or interfere will lead to a decline in the position estimation precision, thus causing deterioration in system performance or even crashes [23]. In an actual drive, the errors during the current sampling process come from different sources. Also, the errors may vary with the structure of the specific drive. The factors that may lead to these errors can be: 1) the errors of the current sensor itself, 2) the parameter error in the signal processing circuits, 3) parameter differences among all current sampling circuits, 4) discrete error in the digital signal processor (DSP), 5) other factors, such as temperature drift, magnetic field interference and so on. Therefore, in an actual drive, it is hard to distinguish those current sensors that encounter accuracy dilemmas from the healthy ones. To conveniently describe this thorny problem regarding current sensor accuracy degradation, the definition of current sensor accuracy uncertainty (SAU) is proposed. There are mainly three types of current SAU problem: 1) offset or biased error; 2) scaling or gain error; 3) random error [24]. At present, the influence of random error is usually eliminated by

Manuscript received April 25, 2019; revised July 6, 2019; accepted August 16, 2019. This work was supported by Shaanxi Science Technology Co-ordination and Innovation Project, China (2013KTCQ01-20, 2016KTCQ01-49). *(Corresponding author: Y. Hu).*

J. Lu and J. Liu are with the School of Automation, Northwestern Polytechnical University (NWPU) and Shaanxi Key Laboratory of Small & Special Electrical Machine and Drive Technology of NWPU, Xi'an 710129, China. (E-mail: j.d.lu@nwpu.edu.cn, jinglinl@nwpu.edu.cn).

Y. Hu and K. Ni are with the Department of Electrical Engineering and Electronics, University of Liverpool, Liverpool L69 3GJ, U.K. (E-mail: y.hu35@liverpool.ac.uk, k.ni@student.Liverpool.ac.uk)

H. Wen is with the Department of Electrical and Electronic Engineering, Xi'an Jiaotong-Liverpool University, Suzhou 215123, China. (E-mail: Huiqing.Wen@xjtlu.edu.cn).

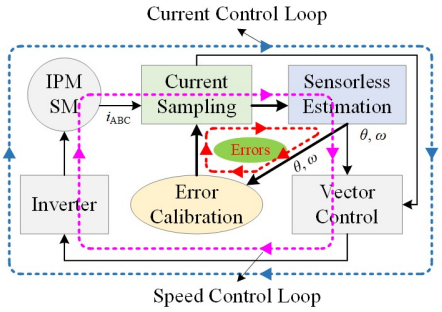

Fig. 1. Multi-error self-circulation loop in sensorless vector controlled IPMSM drives with current SAU problem.

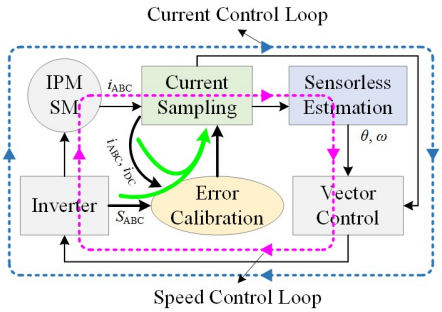

Fig. 2. Proposed multi-error calibration strategy in sensorless vector controlled IPMSM drives.

means of averaging multi-samples. Particularly, if the random error is too large to be eliminated, the system will encounter faults instead of SAU problem, which is out of the scope of this paper. In this paper, the offset and scaling errors will be taken into consideration to eliminate their adverse effects on position estimation. The effect of random error will be discussed in Section VI of this paper.

The offset and scaling errors respectively cause speed and torque ripples with one and two times the fundamental frequency, which have been investigated in [25]-[27]. Usually, the correlation between these sensor errors and system variables are given much attention to eliminate the detrimental effect of current SAU problem on system performance. However, due to the complexity of this correlation, many observers must be added to these error detection strategies. The additionally added observers not only increase the algorithm complexity, but also introduce the problem of response time-delay, thus reducing the feasibility of practical applications. Moreover, if an inertia load is driven, the effectiveness of these calibration methods which much depend on the speed fluctuation information will be threatened. This is because the influence of current SAU problem on the inertia load system mainly reflects on torque ripples rather than speed fluctuation. Whereas it is quite common for an IPMSM drive not to install a torque sensor, which might increase complexity and also cost of the system.

For position sensorless control of IPMSM, the situation can be even more troublesome. This can be explained from three aspects: 1) the current SAU problem will have detrimental effect on position sensorless control; 2) the algorithm of the sensorless control strategies are usually too complicated for an actual drive to further introduce the existing current sensor error calibration methods which are also very complex; 3) there is a contradiction between the sensorless control and current sensor error calibration strategy. The multi-error self-circulation loop in a sensorless vector controlled IPMSM drive with error calibration for current SAU problem by applying conventional strategies is illustrated in Fig.1. In Fig.1, i_{ABC} represent the three-phase currents of the motor; θ and ω are the rotor position and motor angular velocity, respectively.

The contradiction between the sensorless control and current sensor error calibration strategy is illustrated as follows. Accurate rotor position and speed are required for IPMSM drive operation, whereas the current SAU problem deteriorates the accuracy of rotor position and speed estimation. On the other hand, current sensor errors cannot be calibrated effectively without accurate information of rotor speed and position. With this contradiction, the multi-error self-circulation loop in the drive as illustrated in Fig.1 is hard to remove from the system.

Therefore, aimed at solving the aforementioned problem, this paper takes full advantages of the correlation among the multiple current sensors themselves to calibrate the current sampling errors in IPMSM sensorless drives as shown in Fig.2. In Fig.2, i_{DC} represent the DC-bus current; S_{ABC} denotes the switching states of the inverter. In the proposed multi-current-sensor mutual error calibration strategy, no complicated observer is applied, and only the current sampling signals are needed. Also, the most commonly applied seven-segment space vector pulse-width modulation (SVPWM) technology is applied, in which case the total harmonic distortion (THD) is not increased by applying the proposed error calibration strategy.

This paper is organized as follows. In Section II, the impact of current SAU problem on position sensorless control is briefly illustrated. In Section III, the current SAU problem and basic principle for sensor mutual calibration are analyzed. In Sections IV & V, the proposed strategies for balancing of scaling errors and calibrating offset errors for multiple current sensors are illustrated, respectively. In Section VI, the overall control strategy is given. In Section VII, experimental results are presented. The conclusion is given finally in Section VIII.

II. Impact of Current SAU Problem on IPMSM Position Sensorless Control System

The sensorless control technologies for IPMSM drives are generally divided into two categories: saliency based [28]-[31] and model based strategies [32]-[34]. The saliency based methods are usually applied in the low-speed regions, whereas the latter is commonly utilized in the high-speed conditions.

Among all the position sensorless control strategies based on motor saliency, the high frequency (HF) signal injection method is one of the most typical schemes [9]-[11]. A high-pass filter (HPF) or band-pass filter (BPF) is usually required for the system to obtain the HF current response before estimating the rotor position. Therefore, the offset error is filtered out during this process along with the fundamental frequency currents. However, the scaling errors of both the HF and fundamental

frequency currents cannot be eliminated during signal processing, which results in a decline in the position estimation accuracy.

The back electromotive force (EMF) estimation method is one of the model based sensorless control strategies for high-speed operations [12], [32], [33]. However, current measurement errors affect the precision of zero-crossing points (ZCPs) detection, which certainly degrades the position estimation accuracy.

Moreover, sensorless control is not a fully intact control strategy for an IPMSM drive. It means that there must be some other basic control loops for the operations of the drive, e.g., the current and speed control loops for vector control in Fig.2. Sensorless control methods provide the crucial position and speed information for these two control loops. However, aside from these two signals, the three-phase currents are also essential for the vector control. As proven in [27], the offset and scaling errors cause one and two times the fundamental frequency of speed and torque ripples.

All in all, the current SAU problem affects the accuracy of position estimation results and also the drive performance. Therefore, current sensor errors must be calibrated to ensure the drive can operate normally.

III. Current SAU Problem and Basic Principle for Current Sensor Mutual Calibration

Usually an IPMSM drive consists of one bus and two phase current sensors. Taking the current SAU problem into account, the errors in these sensors can be expressed as shown in (1)

$$\begin{cases} i_{\mathrm{ADE}} = k_{\mathrm{A}} \cdot i_{\mathrm{A}} + f_{\mathrm{A}} \\ i_{\mathrm{BDE}} = k_{\mathrm{B}} \cdot i_{\mathrm{B}} + f_{\mathrm{B}} \\ i_{\mathrm{DCDE}} = k_{\mathrm{DC}} \cdot i_{\mathrm{DC}} + f_{\mathrm{DC}} \end{cases} \tag{1}$$

where i_{ADE}, i_{BDE}, i_{DCDE}, i_{A}, i_{B}, and i_{DC} represent the detected (by the current sensors) and actual phase-A, B and DC-bus currents, respectively; k_{A}, k_{B}, k_{DC}, f_{A}, f_{B}, and f_{DC} are the scaling and offset errors of the phase-A, B and DC-bus current sensors, respectively.

From (1), it can be seen that the detected currents do not have determinate relations with the actual ones. This is mainly caused by the uncertain types and values of the multiple current sensor errors. For an ideal case, if all the current sensor errors are eliminated, i.e., $k_{\mathrm{A,\,B,\,DC}} = 1$; $f_{\mathrm{A,\,B,\,DC}} = 0$, all the detected currents will have the same values as those of the actual ones.

The accuracy of position sensorless estimation is highly dependent on the precision of current detection. Therefore, with all these above inevitable uncertain factors existing during the current sampling process, it is hard to guarantee the desired precision for position sensorless control is derived. As a result, in order to obtain accurate and stable position information, it is essential that the precise calibration of all the current sensors must be done prior to the estimation of the rotor position.

This paper takes full advantage of the interrelations of all current sensors for mutual error calibration. The relationships among the measurements from all the current sensors can be developed through the switching states of the inverter, which has been proven by previous literatures and is given in Table I

TABLE I
Relevance of All Current Sensors in Ideal Situation

Switching States	S_{100}	S_{110}	S_{010}	S_{011}	S_{001}	S_{101}
i_{DC}	i_{A}	$-i_{\mathrm{C}}$	i_{B}	$-i_{\mathrm{A}}$	i_{C}	$-i_{\mathrm{B}}$

TABLE II
Relevance of All Current Sensors in Actual Situation

Switching States	i_{ADE}	i_{BDE}	i_{DCDE}
S_{100}	$k_{\mathrm{A}} \cdot i_{\mathrm{A}} + f_{\mathrm{A}}$	$k_{\mathrm{B}} \cdot i_{\mathrm{B}} + f_{\mathrm{B}}$	$k_{\mathrm{DC}} \cdot i_{\mathrm{A}} + f_{\mathrm{DC}}$
S_{110}			$-k_{\mathrm{DC}} \cdot i_{\mathrm{C}} + f_{\mathrm{DC}}$
S_{010}			$k_{\mathrm{DC}} \cdot i_{\mathrm{B}} + f_{\mathrm{DC}}$
S_{011}			$-k_{\mathrm{DC}} \cdot i_{\mathrm{A}} + f_{\mathrm{DC}}$
S_{001}			$k_{\mathrm{DC}} \cdot i_{\mathrm{C}} + f_{\mathrm{DC}}$
S_{101}			$-k_{\mathrm{DC}} \cdot i_{\mathrm{B}} + f_{\mathrm{DC}}$

[26]. In Table I, the subscripts of the six active switching states, S_{100}, …, S_{101}, denote the status of turning on and off (0 is off; 1 is on) of the upper power tube in each bridge arm of the inverter. It should be noted that the interrelation of all the current sensors in Table I is an ideal one, which takes the current SAU problem out of consideration.

However, due to the inevitable current SAU problem, the relevance of all the current sensors in actual situation is given in Table II. It can be seen from Table II that the detected currents, i.e., i_{ADE}, i_{BDE}, and i_{DCDE}, have strong interconnectedness according to switching states. This interconnection feature is also directly related to the errors of the multiple current sensors. Therefore, it is possible to realize current sensor error mutual calibration upon the utilization of this feature. It should be noted that the actual three-phase currents, i.e., i_{A}, i_{B}, and i_{C}, are not constant values, which are changing all the time. Whereas the error types and values in respect of the current SAU problem are relatively invariable even in the scale of minutes.

IV. Balance of Scaling Errors for Multiple Current Sensors

In this paper, the scaling errors are firstly analyzed using the relevance of all current sensors. Then, the scaling error differences are dragged to the same level, which can eliminate the detrimental effects of scaling errors on the position estimation and also normal operation of the drive.

A. Calculation of k_A/K_{DC}

There are four action vectors in one pulse-width modulation (PWM) cycle for the seven-segment PWM strategy. Among the four vectors, only two are active ones. For easy illustrations, the circular output voltage range is usually divided into six sectors (I, …, VI). Vector V_{100} (V_1) is applied in sectors I & VI. The currents of i_{ADE} and i_{DCDE} are both sampled during the action periods of V_1. Because the action period of each active vector is divided into two symmetrical subintervals in each PWM cycle, the sampling points should also be set twice in each PWM cycle for higher detection accuracy. Therefore, in the continuous interval of sectors VI & I, there are many sets of current sampling values (assumed to be $n_{\mathrm{A+}}$ sets), which are given in (2)

$$\begin{cases} i_{\mathrm{ADE}}\left(m_{\mathrm{A+}}\right)=\mathrm{AVG}\left[i_{\mathrm{ADE\_S1}}\left(m_{\mathrm{A+}}\right),i_{\mathrm{ADE\_S2}}\left(m_{\mathrm{A+}}\right)\right] \\ i_{\mathrm{ARE}}\left(m_{\mathrm{A+}}\right)=\mathrm{AVG}\left[i_{\mathrm{ARE\_S1}}\left(m_{\mathrm{A+}}\right),i_{\mathrm{ARE\_S2}}\left(m_{\mathrm{A+}}\right)\right] \\ m_{\mathrm{A+}}=1,\cdots,n_{\mathrm{A+}} \end{cases} \quad (2)$$

where AVG represents the average operation; subscript S_1 and S_2 are the two sampling points in each PWM cycle; $m_{\mathrm{A+}}$ is the sequence number of PWM cycles; i_{ARE} denotes the phase-A current obtained from the DC-bus current sensor.

It should be noted that in (2), $i_{\mathrm{ADE}}(m_{\mathrm{A+}})$ and $i_{\mathrm{ARE}}(m_{\mathrm{A+}})$ are sampled at the same time in each PWM cycle.

Assume that the actual phase-A currents at sampling points S_1 and S_2 are $i_{\mathrm{A\_S1}}(m_{\mathrm{A+}})$ and $i_{\mathrm{A\_S2}}(m_{\mathrm{A+}})$, respectively. The detected currents in each PWM cycle can be expressed as

$$\begin{cases} i_{\mathrm{ADE\_S1}}\left(m_{\mathrm{A+}}\right)=k_{\mathrm{A}}\cdot i_{\mathrm{A\_S1}}\left(m_{\mathrm{A+}}\right)+f_{\mathrm{A}} \\ i_{\mathrm{ADE\_S2}}\left(m_{\mathrm{A+}}\right)=k_{\mathrm{A}}\cdot i_{\mathrm{A\_S2}}\left(m_{\mathrm{A+}}\right)+f_{\mathrm{A}} \\ i_{\mathrm{ARE\_S1}}\left(m_{\mathrm{A+}}\right)=k_{\mathrm{DC}}\cdot i_{\mathrm{A\_S1}}\left(m_{\mathrm{A+}}\right)+f_{\mathrm{DC}} \\ i_{\mathrm{ARE\_S2}}\left(m_{\mathrm{A+}}\right)=k_{\mathrm{DC}}\cdot i_{\mathrm{A\_S2}}\left(m_{\mathrm{A+}}\right)+f_{\mathrm{DC}} \end{cases}. \quad (3)$$

By substituting (3) into (2), we obtain

$$\begin{cases} i_{\mathrm{ADE}}\left(m_{\mathrm{A+}}\right)=k_{\mathrm{A}}\cdot i_{\mathrm{A}}\left(m_{\mathrm{A+}}\right)+f_{\mathrm{A}} \\ i_{\mathrm{ARE}}\left(m_{\mathrm{A+}}\right)=k_{\mathrm{DC}}\cdot i_{\mathrm{A}}\left(m_{\mathrm{A+}}\right)+f_{\mathrm{DC}} \\ i_{\mathrm{A}}\left(m_{\mathrm{A+}}\right)=\mathrm{AVG}\left[i_{\mathrm{A\_S1}}\left(m_{\mathrm{A+}}\right),i_{\mathrm{A\_S2}}\left(m_{\mathrm{A+}}\right)\right] \end{cases}. \quad (4)$$

In order to ensure high precision of current sensor mutual error calibration, the $n_{\mathrm{A+}}$ sets of current values are divided into two groups. *Group* 1: $i_{\mathrm{ADE}}'(n')$ and $i_{\mathrm{ARE}}'(n')$, ($n_{\mathrm{A+}}'$ sets); *Group* 2: $i_{\mathrm{ADE}}''(n'')$ and $i_{\mathrm{ARE}}''(n'')$, ($n_{\mathrm{A+}}''$ sets), which are given in (5)

$$\begin{cases} Group\ 1\begin{cases} i_{\mathrm{ADE}}{}'\left(n'\right),n'=1,...,n_{\mathrm{A+}}{}' \\ i_{\mathrm{ARE}}{}'\left(n'\right),n'=1,...,n_{\mathrm{A+}}{}' \end{cases} \\ Group\ 2\begin{cases} i_{\mathrm{ADE}}{}''\left(n''\right),n''=1,...,n_{\mathrm{A+}}{}'' \\ i_{\mathrm{ARE}}{}''\left(n''\right),n''=1,...,n_{\mathrm{A+}}{}'' \end{cases} \\ n_{\mathrm{A+}}{}'+n_{\mathrm{A+}}{}''=n_{\mathrm{A+}} \end{cases}. \quad (5)$$

The criteria for the division of *Group* 1 & 2 is: For each n'=1, …, $n_{\mathrm{A+}}'$, the value of AVG[$i_{\mathrm{ADE}}'(n')$ + $i_{\mathrm{ARE}}'(n')$] is bigger than the value of AVG[$i_{\mathrm{ADE}}''(n'')$ + $i_{\mathrm{ARE}}''(n'')$] for each n''=1, …, $n_{\mathrm{A+}}''$, which is given in (6)

$$\begin{aligned} &\forall n'\in\left\{1,...,n_{\mathrm{A+}}{}'\right\},\forall n''\in\left\{1,...,n_{\mathrm{A+}}{}''\right\}\Rightarrow \\ &\mathrm{AVG}\left[i_{\mathrm{ADE}}{}'\left(n'\right),i_{\mathrm{ARE}}{}'\left(n'\right)\right]>\mathrm{AVG}\left[i_{\mathrm{ADE}}{}''\left(n''\right),i_{\mathrm{ARE}}{}''\left(n''\right)\right] \end{aligned}. \quad (6)$$

The dividing line ($i_{\mathrm{div\_A}}$) of the two groups is defined in (7)

$$i_{\mathrm{div\_A}}=\frac{1}{n_{\mathrm{A+}}}\sum_{m_{\mathrm{A+}}=1}^{m_{\mathrm{A+}}=n_{\mathrm{A+}}}\mathrm{AVG}\left[i_{\mathrm{ADE}}\left(m_{\mathrm{A+}}\right),i_{\mathrm{ARE}}\left(m_{\mathrm{A+}}\right)\right]. \quad (7)$$

It should be noted that the grouping method of the current sampling values in (5) ~ (7) is just one of the grouping methods. When grouping, we only need to ensure that the current sampling values within the two groups are different. In this grouping method, the sets of the two groups are very hard to be completely the same, which may result in a slight decrease of the compensation accuracy. Therefore, it is more accurate to divide the current values into two groups with a same group set value according to current sampling data, but the calculation may increase greatly in turn due to the high computational complexity of sorting work.

According to the division of the detected currents, the $n_{\mathrm{A+}}$ sets of actual currents $i_{\mathrm{A}}(m_{\mathrm{A+}})$ can also be divided into two corresponding groups $i_{\mathrm{A}}'(n')$ and $i_{\mathrm{A}}''(n'')$:

$$\begin{cases} Group\ 1: i_{\mathrm{A}}{}'\left(n'\right),n'=1,...,n_{\mathrm{A+}}{}' \\ Group\ 2: i_{\mathrm{A}}{}''\left(n''\right),n''=1,...,n_{\mathrm{A+}}{}'' \end{cases}. \quad (8)$$

From (4), (5), and (8), we can obtain:

$$\begin{cases} i_{\mathrm{ADE}}{}'\left(n'\right)=k_{\mathrm{A}}\cdot i_{\mathrm{A}}{}'\left(n'\right)+f_{\mathrm{A}} \\ i_{\mathrm{ARE}}{}'\left(n'\right)=k_{\mathrm{DC}}\cdot i_{\mathrm{A}}{}'\left(n'\right)+f_{\mathrm{DC}} \\ i_{\mathrm{ADE}}{}''\left(n''\right)=k_{\mathrm{A}}\cdot i_{\mathrm{A}}{}''\left(n''\right)+f_{\mathrm{A}} \\ i_{\mathrm{ARE}}{}''\left(n''\right)=k_{\mathrm{DC}}\cdot i_{\mathrm{A}}{}''\left(n''\right)+f_{\mathrm{DC}} \end{cases}. \quad (9)$$

Here, two variables Δi_{ADE} and Δi_{ARE} are defined and derived using (9):

$$\begin{aligned} \Delta i_{\mathrm{ADE}}&=n_{\mathrm{A+}}{}''\cdot\sum_{n'=1}^{n'=n_{\mathrm{A+}}{}'}i_{\mathrm{ADE}}{}'\left(n'\right)-n_{\mathrm{A+}}{}'\cdot\sum_{n''=1}^{n''=n_{\mathrm{A+}}{}''}i_{\mathrm{ADE}}{}''\left(n''\right) \\ &=k_{\mathrm{A}}\cdot\left[n_{\mathrm{A+}}{}''\cdot\sum_{n'=1}^{n'=n_{\mathrm{A+}}{}'}i_{\mathrm{A}}{}'\left(n'\right)-n_{\mathrm{A+}}{}'\cdot\sum_{n''=1}^{n''=n_{\mathrm{A+}}{}''}i_{\mathrm{A}}{}''\left(n''\right)\right] \end{aligned} \quad (10)$$

$$\begin{aligned} \Delta i_{\mathrm{ARE}}&=n_{\mathrm{A+}}{}''\cdot\sum_{n'=1}^{n'=n_{\mathrm{A+}}{}'}i_{\mathrm{ARE}}{}'\left(n'\right)-n_{\mathrm{A+}}{}'\cdot\sum_{n''=1}^{n''=n_{\mathrm{A+}}{}''}i_{\mathrm{ARE}}{}''\left(n''\right) \\ &=k_{\mathrm{DC}}\cdot\left[n_{\mathrm{A+}}{}''\cdot\sum_{n'=1}^{n'=n_{\mathrm{A+}}{}'}i_{\mathrm{A}}{}'\left(n'\right)-n_{\mathrm{A+}}{}'\cdot\sum_{n''=1}^{n''=n_{\mathrm{A+}}{}''}i_{\mathrm{A}}{}''\left(n''\right)\right] \end{aligned} \quad (11)$$

From (10) and (11), it can be seen that the value of Δi_{ADE} and Δi_{ARE} can be calculated by the existing variables. According to (10) and (11), we obtain the relationship between k_{A} and k_{DC}:

$$\frac{k_{\mathrm{A}}}{k_{\mathrm{DC}}}=\frac{\Delta i_{\mathrm{ADE}}}{\Delta i_{\mathrm{ARE}}}. \tag{12}$$

B. Calculation of k_B/K_{DC}

Vector V_{010} (V_3) is applied in sectors II & III. The current of i_{BDE} and i_{DCDE} are both sampled during the action periods of V_3. The sampling points should also be set twice in each PWM cycle for higher detection accuracy. In the continuous interval of sectors II & III, there are many sets of current sampling values (assumed to be n_{B} sets), which are given in (13)

$$\begin{cases} i_{\mathrm{BDE}}\left(m_{\mathrm{B}}\right)=k_{\mathrm{B}}\cdot i_{\mathrm{B}}\left(m_{\mathrm{B}}\right)+f_{\mathrm{B}} \\ i_{\mathrm{BRE}}\left(m_{\mathrm{B}}\right)=k_{\mathrm{DC}}\cdot i_{\mathrm{B}}\left(m_{\mathrm{B}}\right)+f_{\mathrm{DC}} \\ i_{\mathrm{B}}\left(m_{\mathrm{B}}\right)=\mathrm{AVG}\left[i_{\mathrm{B\_S1}}\left(m_{\mathrm{B}}\right),i_{\mathrm{B\_S2}}\left(m_{\mathrm{B}}\right)\right] \\ m_{\mathrm{B}}=1,\cdots,n_{\mathrm{B}} \end{cases} \tag{13}$$

where m_{B} is the sequence number of PWM cycles; i_{BRE} denotes the phase-B current obtained from the DC-bus current sensor.

The n_{B} sets of phase-B currents are also divided into two groups. *Group* 1: $i_{\mathrm{BDE}}'(n')$ and $i_{\mathrm{BRE}}'(n')$, (n_{B}' sets); *Group* 2: $i_{\mathrm{BDE}}''(n'')$ and $i_{\mathrm{BRE}}''(n'')$, (n_{B}'' sets), which are given in (14)

$$\begin{cases} \mathit{Group}\ 1\begin{cases} {i_{\mathrm{BDE}}}'\left(n'\right),n'=1,...,{n_{\mathrm{B}}}' \\ {i_{\mathrm{BRE}}}'\left(n'\right),n'=1,...,{n_{\mathrm{B}}}' \end{cases} \\ \mathit{Group}\ 2\begin{cases} {i_{\mathrm{BDE}}}''\left(n''\right),n''=1,...,{n_{\mathrm{B}}}'' \\ {i_{\mathrm{BRE}}}''\left(n''\right),n''=1,...,{n_{\mathrm{B}}}'' \end{cases} \\ {n_{\mathrm{B}}}'+{n_{\mathrm{B}}}''=n_{\mathrm{B}} \end{cases}. \tag{14}$$

The criteria for the division of *Group* 1 & 2 for phase-B current is similar to that of phase-A. According to the division of the detected currents, the n_{B} sets of actual currents $i_{\mathrm{B}}(m_{\mathrm{B}})$ are also divided into two corresponding groups $i_{\mathrm{B}}'(n')$ and $i_{\mathrm{B}}''(n'')$:

$$\begin{cases} \mathit{Group}\ 1:{i_{\mathrm{B}}}'\left(n'\right),n'=1,...,{n_{\mathrm{B}}}' \\ \mathit{Group}\ 2:{i_{\mathrm{B}}}''\left(n''\right),n''=1,...,{n_{\mathrm{B}}}'' \end{cases}. \tag{15}$$

Similarly, two variables Δi_{BDE} and Δi_{BRE} are defined:

$$\begin{aligned} \Delta i_{\mathrm{BDE}} &= {n_{\mathrm{B}}}''\cdot\sum_{n'=1}^{n'={n_{\mathrm{B}}}'}{i_{\mathrm{BDE}}}'\left(n'\right)-{n_{\mathrm{B}}}'\cdot\sum_{n''=1}^{n''={n_{\mathrm{B}}}''}{i_{\mathrm{BDE}}}''\left(n''\right) \\ &= k_{\mathrm{B}}\cdot\left[{n_{\mathrm{B}}}''\cdot\sum_{n'=1}^{n'={n_{\mathrm{B}}}'}{i_{\mathrm{B}}}'\left(n'\right)-{n_{\mathrm{B}}}'\cdot\sum_{n''=1}^{n''={n_{\mathrm{B}}}''}{i_{\mathrm{B}}}''\left(n''\right)\right] \end{aligned} \tag{16}$$

$$\begin{aligned} \Delta i_{\mathrm{BRE}} &= {n_{\mathrm{B}}}''\cdot\sum_{n'=1}^{n'={n_{\mathrm{B}}}'}{i_{\mathrm{BRE}}}'\left(n'\right)-{n_{\mathrm{B}}}'\cdot\sum_{n''=1}^{n''={n_{\mathrm{B}}}''}{i_{\mathrm{BRE}}}''\left(n''\right) \\ &= k_{\mathrm{DC}}\cdot\left[{n_{\mathrm{B}}}''\cdot\sum_{n'=1}^{n'={n_{\mathrm{B}}}'}{i_{\mathrm{B}}}'\left(n'\right)-{n_{\mathrm{B}}}'\cdot\sum_{n''=1}^{n''={n_{\mathrm{B}}}''}{i_{\mathrm{B}}}''\left(n''\right)\right] \end{aligned} \tag{17}$$

From (16) and (17), it can be seen that the values of Δi_{BDE} and Δi_{BRE} can be calculated by the existing variables. According to (16) and (17), we obtain the relationship between k_{B} and k_{DC}:

$$\frac{k_{\mathrm{B}}}{k_{\mathrm{DC}}}=\frac{\Delta i_{\mathrm{BDE}}}{\Delta i_{\mathrm{BRE}}}. \tag{18}$$

C. Balance of Scaling Errors

Combining (12) and (18), the relations among all the scaling errors can be finally obtained:

$$\begin{aligned} &k_{\mathrm{A}}:k_{\mathrm{B}}:k_{\mathrm{DC}} \\ &=\left(\Delta i_{\mathrm{ADE}}\cdot\Delta i_{\mathrm{BRE}}\right):\left(\Delta i_{\mathrm{ARE}}\cdot\Delta i_{\mathrm{BDE}}\right):\left(\Delta i_{\mathrm{ARE}}\cdot\Delta i_{\mathrm{BRE}}\right) \end{aligned}. \tag{19}$$

Therefore, the compensation parameters of the scaling errors, $k_{\mathrm{A\_Com}}$, $k_{\mathrm{B\_Com}}$, and $k_{\mathrm{DC\_Com}}$, can be obtained:

$$\begin{cases} k_{\mathrm{A\_Com}}=\dfrac{k_{\mathrm{Avg}}}{\Delta i_{\mathrm{ADE}}\cdot\Delta i_{\mathrm{BRE}}} \\ k_{\mathrm{B\_Com}}=\dfrac{k_{\mathrm{Avg}}}{\Delta i_{\mathrm{ARE}}\cdot\Delta i_{\mathrm{BDE}}} \\ k_{\mathrm{DC\_Com}}=\dfrac{k_{\mathrm{Avg}}}{\Delta i_{\mathrm{ARE}}\cdot\Delta i_{\mathrm{BRE}}} \\ k_{\mathrm{Avg}}=\dfrac{\Delta i_{\mathrm{ADE}}\cdot\Delta i_{\mathrm{BRE}}+\Delta i_{\mathrm{ARE}}\cdot\Delta i_{\mathrm{BDE}}+\Delta i_{\mathrm{ARE}}\cdot\Delta i_{\mathrm{BRE}}}{3} \end{cases}. \tag{20}$$

If the detected currents i_{ADE}, i_{BDE}, and i_{DCDE} are multiplied by the corresponding compensation parameters $k_{\mathrm{A\_Com}}$, $k_{\mathrm{B\_Com}}$, and $k_{\mathrm{DC\_Com}}$, the scaling errors of the three current sensors can be dragged to the same level k_{Avg}, thus the detrimental effects of scaling error differences on position estimation and system performance can be finally eliminated.

V. Calibration of Offset Errors

Vector V_{011} (V_4) is applied in sectors III & IV. The current of i_{ADE} and i_{DCDE} are both sampled during each action period of V_4. The sampling points should also be set twice in each PWM cycle for higher detection accuracy. In the continuous interval of sectors III & IV, there are many sets of current sampling values (assumed to be $n_{\mathrm{A-}}$ sets), which are given in (21)

$$\begin{cases} i_{\mathrm{ADE-}}\left(m_{\mathrm{A-}}\right)=k_{\mathrm{A}}\cdot i_{\mathrm{A-}}\left(m_{\mathrm{A-}}\right)+f_{\mathrm{A}} \\ i_{\mathrm{ARE-}}\left(m_{\mathrm{A-}}\right)=k_{\mathrm{DC}}\cdot i_{\mathrm{A-}}\left(m_{\mathrm{A-}}\right)-f_{\mathrm{DC}} \\ m_{\mathrm{A-}}=1,\cdots,n_{\mathrm{A-}} \end{cases} \tag{21}$$

where $i_{\mathrm{ADE-}}$ and $i_{\mathrm{ARE-}}$ are the phase-A currents obtained from phase-A and DC-bus current sensors, respectively; $m_{\mathrm{A-}}$ denotes the sequence number of PWM cycles; $i_{\mathrm{A-}}$ represents the actual phase-A current.

By substituting (12) into (4), we can obtain:

$$\begin{aligned} &\Delta i_{\mathrm{ARE}}\cdot i_{\mathrm{ADE}}\left(m_{\mathrm{A+}}\right)-\Delta i_{\mathrm{ADE}}\cdot i_{\mathrm{ARE}}\left(m_{\mathrm{A+}}\right) \\ &=\Delta i_{\mathrm{ARE}}\cdot f_{\mathrm{A}}-\Delta i_{\mathrm{ADE}}\cdot f_{\mathrm{DC}} \end{aligned}. \tag{22}$$

Here, we define parameter $\Delta i_{\mathrm{A+}}$ as:

$$\Delta i_{\mathrm{A+}}=\frac{\Delta i_{\mathrm{ARE}}\cdot\sum_{m_{\mathrm{A+}}=1}^{m_{\mathrm{A+}}=n_{\mathrm{A+}}} i_{\mathrm{ADE}}\left(m_{\mathrm{A+}}\right)-\Delta i_{\mathrm{ADE}}\cdot\sum_{m_{\mathrm{A+}}=1}^{m_{\mathrm{A+}}=n_{\mathrm{A+}}} i_{\mathrm{ARE}}\left(m_{\mathrm{A+}}\right)}{n_{\mathrm{A+}}}. \tag{23}$$

From (23), it can be seen that the value of $\Delta i_{\mathrm{A+}}$ can be calculated by the existing variables.

By simplifying (23) and taking advantage of (22), we obtain:

$$\begin{aligned} \Delta i_{\mathrm{A+}}&=\frac{\sum_{m_{\mathrm{A+}}=1}^{m_{\mathrm{A+}}=n_{\mathrm{A+}}}\left[\Delta i_{\mathrm{ARE}}\cdot i_{\mathrm{ADE}}\left(m_{\mathrm{A+}}\right)-\Delta i_{\mathrm{ADE}}\cdot i_{\mathrm{ARE}}\left(m_{\mathrm{A+}}\right)\right]}{n_{\mathrm{A+}}} \\ &=\frac{\sum_{m_{\mathrm{A+}}=1}^{m_{\mathrm{A+}}=n_{\mathrm{A+}}}\left[\Delta i_{\mathrm{ARE}}\cdot f_{\mathrm{A}}-\Delta i_{\mathrm{ADE}}\cdot f_{\mathrm{DC}}\right]}{n_{\mathrm{A+}}} \\ &=\Delta i_{\mathrm{ARE}}\cdot f_{\mathrm{A}}-\Delta i_{\mathrm{ADE}}\cdot f_{\mathrm{DC}} \end{aligned}. \tag{24}$$

Similarly, we define parameter $\Delta i_{\mathrm{A-}}$ as:

$$\Delta i_{\mathrm{A-}}=\frac{\Delta i_{\mathrm{ARE}}\cdot\sum_{m_{\mathrm{A-}}=1}^{m_{\mathrm{A-}}=n_{\mathrm{A-}}} i_{\mathrm{ADE-}}\left(m_{\mathrm{A-}}\right)-\Delta i_{\mathrm{ADE}}\cdot\sum_{m_{\mathrm{A-}}=1}^{m_{\mathrm{A-}}=n_{\mathrm{A-}}} i_{\mathrm{ARE-}}\left(m_{\mathrm{A-}}\right)}{n_{\mathrm{A-}}}. \tag{25}$$

From (25), it can be seen that the value of $\Delta i_{\mathrm{A-}}$ can also be calculated by the existing variables.

By substituting (12) into (21), we can obtain:

$$\begin{aligned} &\Delta i_{\mathrm{ARE}}\cdot i_{\mathrm{ADE-}}\left(m_{\mathrm{A-}}\right)-\Delta i_{\mathrm{ADE}}\cdot i_{\mathrm{ARE-}}\left(m_{\mathrm{A-}}\right) \\ &=\Delta i_{\mathrm{ARE}}\cdot f_{\mathrm{A}}+\Delta i_{\mathrm{ADE}}\cdot f_{\mathrm{DC}} \end{aligned}. \tag{26}$$

By simplifying (25) and taking advantage of (26), we obtain:

$$\begin{aligned} \Delta i_{\mathrm{A-}}&=\frac{\sum_{m_{\mathrm{A-}}=1}^{m_{\mathrm{A-}}=n_{\mathrm{A-}}}\left[\Delta i_{\mathrm{ARE}}\cdot i_{\mathrm{ADE-}}\left(m_{\mathrm{A-}}\right)-\Delta i_{\mathrm{ADE}}\cdot i_{\mathrm{ARE-}}\left(m_{\mathrm{A-}}\right)\right]}{n_{\mathrm{A-}}} \\ &=\frac{\sum_{m_{\mathrm{A-}}=1}^{m_{\mathrm{A-}}=n_{\mathrm{A-}}}\left[\Delta i_{\mathrm{ARE}}\cdot f_{\mathrm{A}}+\Delta i_{\mathrm{ADE}}\cdot f_{\mathrm{DC}}\right]}{n_{\mathrm{A-}}} \\ &=\Delta i_{\mathrm{ARE}}\cdot f_{\mathrm{A}}+\Delta i_{\mathrm{ADE}}\cdot f_{\mathrm{DC}} \end{aligned}. \tag{27}$$

Combining (24) and (27), we obtain:

$$\begin{cases} f_{\mathrm{A}}=\dfrac{\Delta i_{\mathrm{A+}}+\Delta i_{\mathrm{A-}}}{2\Delta i_{\mathrm{ARE}}} \\ f_{\mathrm{DC}}=\dfrac{-\Delta i_{\mathrm{A+}}+\Delta i_{\mathrm{A-}}}{2\Delta i_{\mathrm{ADE}}} \end{cases}. \tag{28}$$

Similarly, we define parameter Δi_{B} as:

$$\Delta i_{B}=\frac{\Delta i_{\mathrm{BRE}}\cdot\sum_{m_{B}=1}^{m_{B}=n_{B}} i_{\mathrm{BDE}}\left(m_{B}\right)-\Delta i_{\mathrm{BDE}}\cdot\sum_{m_{B}=1}^{m_{B}=n_{B}} i_{\mathrm{BRE}}\left(m_{B}\right)}{n_{B}}. \tag{29}$$

From (29), it can be seen that the value of Δi_{B} can also be calculated by the existing variables.

By substituting (18) into (13), we can obtain:

$$\begin{aligned} &\Delta i_{\mathrm{BRE}}\cdot i_{\mathrm{BDE}}\left(m_{\mathrm{B}}\right)-\Delta i_{\mathrm{BDE}}\cdot i_{\mathrm{BRE}}\left(m_{\mathrm{B}}\right) \\ &=\Delta i_{\mathrm{BRE}}\cdot f_{\mathrm{B}}-\Delta i_{\mathrm{BDE}}\cdot f_{\mathrm{DC}} \end{aligned}. \tag{30}$$

By simplifying (29) and taking advantage of (30), we obtain:

$$\Delta i_{B}=\Delta i_{\mathrm{BRE}}\cdot f_{\mathrm{B}}-\Delta i_{\mathrm{BDE}}\cdot f_{\mathrm{DC}}. \tag{31}$$

Combining (28) and (31), we obtain:

$$f_{\mathrm{B}}=\frac{\Delta i_{\mathrm{BDE}}\cdot f_{\mathrm{DC}}+\Delta i_{B}}{\Delta i_{\mathrm{BRE}}}. \tag{32}$$

The offset errors of the three current sensors are all calculated according to (28) and (32), thus the detrimental effects of offset errors on position estimation and system performance can be finally eliminated.

It should be noted that the selection of the basic vectors and the corresponding compensation strategy are dependent on the preinstallation of the current sensors. That is, if the specific installation method of the current sensors is different from the aforementioned one, the selected basic vectors along with the corresponding calculation method should be modified. Whereas the compensation strategy is similar.

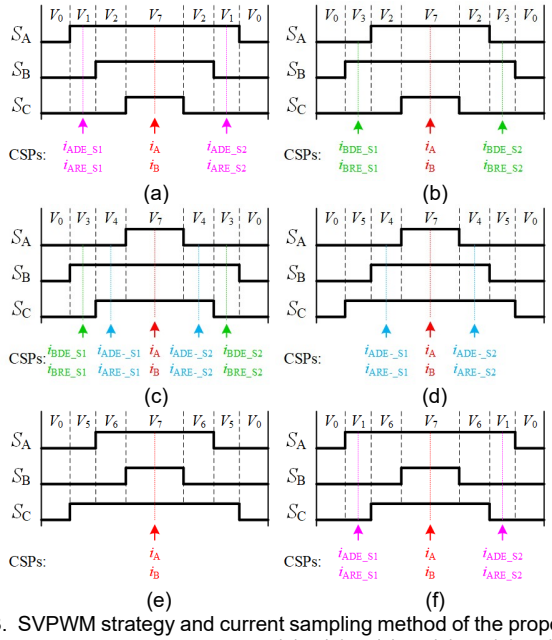

Fig. 3. SVPWM strategy and current sampling method of the proposed error calibration strategy in sectors: (a) I, (b) II, (c) III, (d) IV, (e) V, (f) VI.

VI. Overall Control Strategy

From the analysis of Sections VI & V, it can be seen that the operation of error calibration for current SAU problem only utilizes several sets of current sampling values. The commonly used SVPWM strategy can be applied in the proposed strategy, which can be illustrated in Fig.3. In Fig.3, CSPs represent the multiple current sampling points, where the CSPs marked by red i_A and i_B at the middle of each PWM cycle are used for signal feedback of vector control. The dead time is a practical issue for motor drives, which can affect the output voltage vector. However, the dead time will not affect the accuracy of the proposed current sensor error calibration strategy as long as the switching action period of the inverter is completed. It should be noted that due to the existence of switching device dead time, diode recovery time, AD sampling time and so on, there must be a minimum action period of T_{min} for effective current sampling of the CSPs with pink, green and blue marks. If any of these CSPs (except those with red marks) is with the action period shorter than T_{min}, they will be removed.

Another thing that should be noted is the influence of random error on the proposed error calibration strategy for current SAU problem. It can be seen from the above Sections that more than one set of current signals are sampled and analyzed for the proposed strategy, i.e., n_{A+} sets of currents i_{ADE} and i_{ARE}; n_B sets of currents i_{BDE} and i_{BRE}; n_{A-} sets of currents i_{ADE-} and i_{ARE-}. The random errors can be filtered out by averaging the effects of these multi-samples.

It should be noted that the accuracy of the proposed current error calibration strategy is dependent on the sets of current sampling values. Therefore, in order to guarantee a high compensation accuracy, the number of current values should not be very small. In the normal operation of the drive, taking the high PWM switching frequency and current sampling frequency into consideration, when the output voltage vector passes all the required sectors, the current sampling values will be sufficient for the calibration purpose. However, in some unknown conditions, if the number of sampling currents is not large enough, we can pre-set a parameter of the minimum number of sampling data in advance in actual applications. The calculation will not be carried out unless the number of the current sampling values meet this requirement.

It should also be pointed out that the output voltage modulation area will be one of the key factors that affect the accuracy of the compensation strategy. This is because in the low modulation area, usually the action time of the basic vectors is very short, which is contrary to the requirement of the action time of the basic vectors. Another factor that may affect the accuracy of the proposed compensation strategy is the operation current value. Therefore, in order to ensure the accuracy of the proposed strategy, the differences between the current values in the two divided groups should be large enough. Therefore, the load condition may also affect the accuracy of the calibration results - a heavier load may result in a higher calibration accuracy.

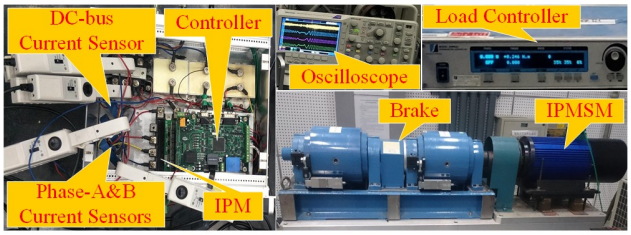

Fig. 4. Experiment setup.

TABLE III
Main Parameters of IPMSM for Experiment.

Parameter	Value	Parameter	Value
Rated power	5 kW	Pole pairs	3
Inverter DC voltage	540 V	*d*-axis Inductance	4.2 mH
Rated voltage	380 V	*q*-axis Inductance	10.1 mH
Rated current	8.5 A	Phase resistance	0.18 Ω
Efficiency	0.9	Maximum speed	3000 r/min
Rated torque	15 N·m		

VII. Experimental Validation

In order to verify the effectiveness of the proposed error calibration strategy for current SAU problem in IPMSM drives, an experiment setup is built as given in Fig.4. The main parameters of the IPMSM prototype are given in Table III. The system is powered by a three-phase 380 V alternating current (AC) source with a multi-level converter. The inverter is an integrated power module (IPM), Mitsubishi PM75RLA120, with the switching frequency of 8 kHz. The current sensors used in the drive are isolated hall-effect ones (HS01-100, maximum sample rate 100 kHz). The sensorless estimation method is based on the rotating HF voltage injection, with the injected frequency of 1 kHz and voltage of 30 V.

In order to imitate the current SAU problem, the sensor errors are artificially added to the software. The six sensor error parameters are given in Table IV. In order to test the performance of the proposed current sensor error calibration strategy for high-precision position sensorless control, the motor is firstly controlled at 300 rpm with a full load of 15 N·m. And for comparison purpose, both the system performances

TABLE IV
PARAMETERS OF SENSOR ERRORS.

Parameter	Value	Parameter	Value
k_A	1.2	f_A	1.75 A
k_B	0.9	f_B	1.5 A
k_{DC}	0.85	f_{DC}	-2.0 A

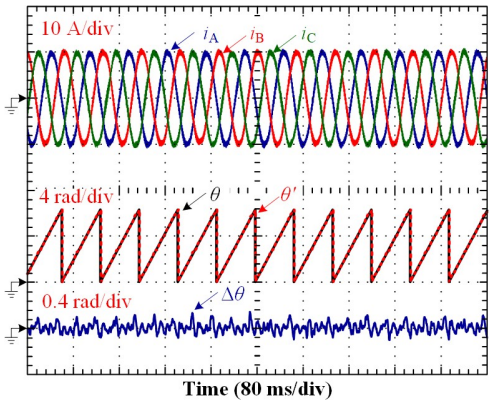

Fig. 5. Sensorless estimation with all current sensors healthy.

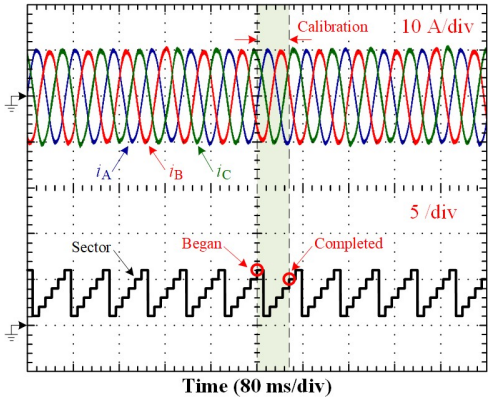

Fig. 6. Original three-phase currents and output voltage sectors before artificially added current SAU problem.

with all current sensors healthy and sensors with errors are tested. In Fig.5, the experimental results of the sensorless estimation with all current sensors in healthy conditions are presented. In the figure, θ, θ' and $\Delta\theta$ are the actual, estimated and estimation error of rotor position, respectively. It can be seen that the estimated position follows the actual one accurately, with a small estimation error of about ±0.16 rad.

If the sensor errors are taken into consideration, as displayed in Fig.6, the original three-phase currents and output voltage sectors are illustrated. The errors are artificially added to the software at the beginning of the experiment for comparison, which are presented in Fig.7. In Fig.7, i_A', i_B' and i_C' are the three-phase currents obtained after the artificially added sensor errors, and $\Delta i_A'$, $\Delta i_B'$ and $\Delta i_C'$ are the three-phase current errors compared to the original ones. The calibration process takes place from the middle of the scope that begins at the boundary between sectors V and VI and ends at the boundary between sectors IV and V. It can be seen that the three-phase currents before error calibration show very big differences from the original ones, and the errors are determined by the artificially introduced six parameters in Table IV.

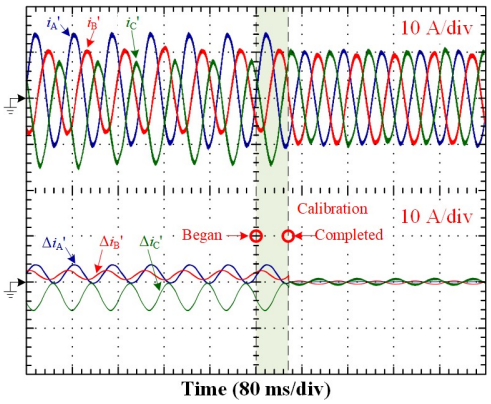

Fig. 7. Three-phase currents after artificially added sensor errors and calibration process for current SAU problem

TABLE V
MAIN VARIABLES DURING SENSOR ERRORS CALIBRATION PROCESS.

Parameter	Value	Parameter	Value
Δi_{ADE}	41010 A	Δi_{BDE}	30846 A
Δi_{ARE}	29073 A	Δi_{BRE}	29121 A
Δi_{A+}	133132 A^2	Δi_{A-}	-31090 A^2
Δi_B	105404 A^2		
k_{A_Com}	0.82	f_{A_Cali}	1.75 A
k_{B_Com}	1.09	f_{B_Cali}	1.50 A
k_{DC_Com}	1.16	f_{DC_Cali}	-2.00 A
$k_A \cdot k_{A\_Com}$	0.984	$k_B \cdot k_{B\_Com}$	0.981
$k_{DC} \cdot k_{DC\_Com}$	0.986		

Therefore, in order to compensate the errors, the sensor mutual calibration strategy is implemented from the middle of the scope. After the calibration process is completed, the three-phase currents with artificially added sensor errors are pulled back to a higher accuracy compared to that before the calibration process. The calibration process begins with the output voltage sector of VI, and then passes sectors I, II, III and IV in sequence. Many sets of current values are obtained as a result. By dealing with these current data, the main variables can be calculated by using the proposed strategy, which are given in Table V. Finally, the six sensor error parameters are estimated. From Table IV and Table V, it can be seen that the proposed sensor error calibration strategy has high estimation accuracy. One reason is that the random error effects are eliminated by the obtained multiple sets of current values. It should be noted that the offset errors of all the current sensors can be precisely detected as long as the number of sampling data is large enough. Whereas the scaling errors are hard to be completely compensated, which is the limitation of the proposed strategy.

In Fig.8, the sensorless estimation results of the three-phase currents with artificially added sensor errors are presented. Compared with the estimation results in Fig.7, it can be seen that the estimation error before error calibration increases obviously, which is about ±0.24 rad. After the error calibration, the estimation error is pulled back to the same level as in all sensor healthy condition, which is about ±0.16 rad.

In Fig.9 and Fig.10, the experimental results of the sensorless control in the dynamic conditions are displayed. The motor operates at 500 rpm with load of 10 N·m at the beginning. At 2s, the speed command changed to 100 rpm and then back to 500 rpm at 6 s. A load of 7 N·m is removed from the motor shaft at

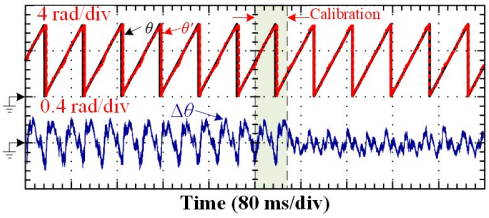

Fig. 8. Sensorless estimation results using i_A', i_B' and i_C' in Fig.7.

10 s and then added back at 16 s. From the results it can be seen that due to the existing current sampling errors, the estimation error can only be controlled within about ±0.25 rad. By applying the proposed current sensor error calibration strategy, the estimation error is controlled within about ±0.15 rad. The accuracy of the position estimation result is improved.

VIII. Conclusion

Current SAU problem causes a decline in position estimation precision for IPMSM sensorless drives. The current sensor error calibration strategies proposed in the previous literatures have obvious limitations regarding sensorless control applications. Based on the correlation among the multiple current sensors, in this paper, the proposed multiple current sensor mutual error calibration strategy has many advantages, which can be summarized as follows:

1) The algorithm is simple enough not to add additional computational burden to the IPMSM sensorless drives that already have very heavy computational burdens. Therefore, the proposed strategy is more applicable in actual situations.
2) There is no need to change the PWM synthesis strategy for the implementation of the proposed strategy. As a result, it has all advantages of SVPWM technology.
3) For an IPMSM sensorless drive with current SAU problem, the proposed strategy does not have a multi-error self-circulation loop that may exist in previous calibration strategies.
4) Thanks to the multi-sets of current sampling signals, the proposed strategy can also eliminate the influence of random error.
5) For an IPMSM drive with three independent phase current sensors or with a position sensor installed, the proposed error calibration strategy for current SAU problem can also be extended in a similar way.
6) Better performance can be achieved by using current sensors with higher bandwidth, whereas the performance improvement is limited, and the cost is greatly increased. Therefore, this is a comprehensive consideration between the performance and cost.

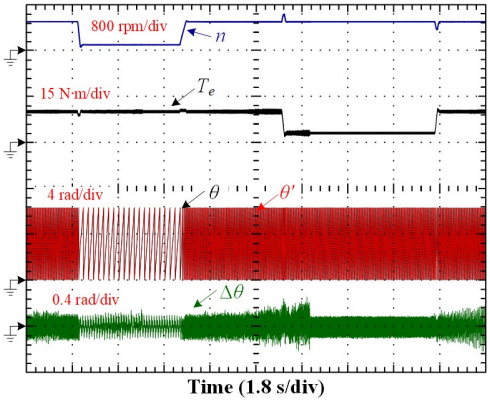

Fig. 9. Sensorless results without the proposed calibration strategy.

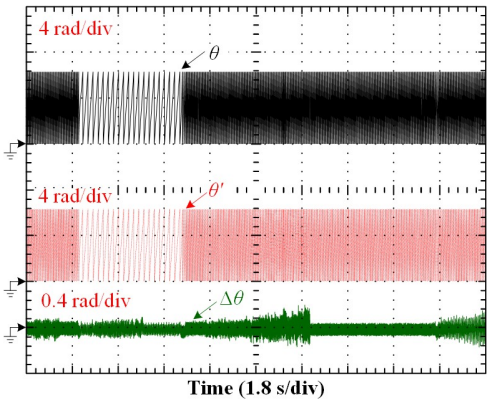

Fig. 10. Sensorless results using the proposed calibration strategy.

References

[1] M. Siami, D. A. Khaburi and J. Rodríguez, "Torque Ripple Reduction of Predictive Torque Control for PMSM Drives With Parameter Mismatch," *IEEE Trans. Power Electron.,* vol. 32, no. 9, pp. 7160-7168, Sep. 2017.

[2] C. Gong, Y. H. Hu, G. P. Chen, H. Q. Wen, Z. Wang and K. Ni, "A DC-bus capacitor discharge strategy for PMSM drive system with large inertia and small system safe current in EVs," *IEEE Transactions on Ind. Infor.*, DOI: 10.1109/TII.2019.2895317, 2019.

[3] Z. Q. Wang, A. B. Yu, X. M. Li, G. Z. Zhang, and C. L. Xia, "A novel current predictive control based on fuzzy algorithm for PMSM," *IEEE J. Em. Sel. Top. P.,* DOI: 10.1109/JESTPE.2019.2902634, 2019.

[4] C. Gan, Q. G. Sun, J. H. Wu, W. B. Kong, C. W. Shi and Y. H. Hu, "MMC-based SRM drives with decentralized battery energy storage system for hybrid electric vehicles," *IEEE Trans. Power Electron.,* vol. 34, no. 3, pp. 2608-2621, Mar. 2019.

[5] Y. H. Hu, C. Gan, Q. G. Sun, P. Li, J. H. Wu and H. Q. Wen, "Modular tri-port high-power converter for SRM based plug-in hybrid electrical trucks," *IEEE Trans. Power Electron.,* vol. 33, no. 4, pp. 3247-3257, Apr. 2018.

[6] Z. Wang, Y. B. Wang, J. Chen, and M. Cheng, "Fault-Tolerant Control of NPC Three-Level Inverters-Fed Double-Stator-Winding PMSM Drives Based on Vector Space Decomposition," *IEEE Trans. Ind. Electron.*, vol. 64, no. 11, pp. 8446-8458, Nov. 2017.

[7] J. L. Liu, C. Gong, Z. X. Han, and H. Z. Yu, "IPMSM model predictive control in flux-weakening operation using an improved algorithm," *IEEE Trans. Ind. Electron.*, vol. 65, no. 12, pp. 9378-9387, Dec. 2018.

[8] S. K. Kommuri, S. B. Lee and K. C. Veluvolu, "Robust sensors-fault-tolerance with sliding mode estimation and control for PMSM drives," *IEEE/ASME Trans. Mechatronics*, vol. 23, no. 1, pp. 17-28, Feb. 2018.

[9] A. Yousefi-Talouki, P. Pescetto, G. Pellegrino and I. Boldea, "Combined active flux and high-frequency injection methods for sensorless direct-flux vector control of synchronous reluctance machines," *IEEE Trans. Power Electron.,* vol. 33, no. 3, pp. 2447-2457, Mar. 2018.

[10] M. X. Bui, D. Q. Guan, D. Xiao, and M. Faz Rahman, "A modified sensorless control scheme for interior permanent magnet synchronous motor over zero to rated speed range using current derivative measurements," *IEEE Trans. Ind. Electron.*, vol. 66, no. 1, pp. 102-113, Jan. 2019.

[11] G. L. Wang, H. L. Zhou, N. N. Zhao, C. R. Li, and D. G. Xu, "Sensorless control of IPMSM drives using pseudo-random phase-switching fixed-frequency signal injection scheme," *IEEE Trans. Ind. Electron.,* vol. 65, no. 10, pp. 7660-7671, Oct. 2018.

[12] H. L. Zhan, Z. Q. Zhu and M. Odavic, "Nonparametric sensorless drive method for open-winding PMSM based on zero-sequence back EMF with circulating current suppression," *IEEE Trans. Power Electron.,* vol. 32, no. 5, pp. 3808-3817, May 2017.
[13] S. Nalakath, Y. G. Sun, M. Preindl and A. Emadi, "Optimization-based position sensorless finite control set model predictive control for IPMSMs," *IEEE Trans. Power Electron.,* vol. 33, no. 10, pp. 8672-8682, Oct. 2018.
[14] J. Choi, K. Nam, A. A. Bobtsov and R. Ortega, "Sensorless control of IPMSM based on regression model," *IEEE Trans. Power Electron.,* DOI: 10.1109/TPEL.2018.2883303, 2018.
[15] G. L. Wang, R. Liu, N. N. Zhao, D. W. Ding and D. G. Xu, "Enhanced linear ADRC strategy for HF pulse voltage signal injection-based sensorless IPMSM drives," *IEEE Trans. Power Electron.,* vol. 34, no. 1, pp. 514-525, Jan. 2019.
[16] R. A. Fantino, C. A. Busada and J. A. Solsona, "Observer-based grid-voltage sensorless synchronization and control of a VSI-LCL tied to an unbalanced grid," *IEEE Trans. Ind. Electron.,* vol. 66, no. 7, pp. 4972-4981, Jul. 2019.
[17] P. L. Xu and Z. Q. Zhu, "Initial rotor position estimation using zero-sequence carrier voltage for permanent-magnet synchronous machines," *IEEE Trans. Ind. Electron.,* vol. 64, no. 1, pp. 149-158, Jan. 2017.
[18] S. G. Jorge, C. A. Busada and J. Solsona, "Low computational burden grid voltage sensorless current controller," *IET Power Electron.,* vol. 6, no. 8, pp. 1592-1599, Sep. 2013.
[19] C. D. Angelo, G. Bossio, J. Solsona, G. O. García and M. I. Valla, "A rotor position and speed observer for permanent-magnet motors with nonsinusoidal EMF waveform," *IEEE Trans. Ind. Electron.,* vol. 52, no. 3, pp. 807-813, June 2005.
[20] G. L. Wang, J. Y. Kuang, N. N. Zhao, G. Q. Zhang and D. G. Xu, "Rotor position estimation of PMSM in low-speed region and standstill using zero-voltage vector injection," *IEEE Trans. Power Electron.,* vol. 33, no. 9, pp. 7948-7958, Sep. 2018.
[21] D. G. Forchetti, G. O. García and M. I. Valla, "Adaptive observer for sensorless control of stand-alone doubly fed induction generator," *IEEE Trans. Ind. Electron.,* vol. 56, no. 10, pp. 4174-4180, Oct. 2009.
[22] K. R. Cho and J. K. Seok, "Correction on current measurement errors for accurate flux estimation of AC drives at low stator frequency," *IEEE Trans. Ind. Appl.,* vol. 44, no. 2, pp. 594-603, Mar./Apr., 2008.
[23] M. C. Harke and R. D. Lorenz, "The spatial effect and compensation of current sensor differential gains for three-phase three-wire systems," *IEEE Trans. Ind. Appl.,* vol. 44, no. 4, pp. 1181-1189, Jul./Aug., 2008.
[24] Q. N. Trinh, P. Wang, Y. Tang, L. H. Koh and F. H. Choo, "Compensation of DC offset and scaling errors in voltage and current measurements of three-phase AC/DC converters," *IEEE Trans. Power Electron.,* vol. 33, no. 6, pp. 5401-5414, June 2018.
[25] M. Kim, S. K. Sul and J. Lee, "Compensation of current measurement error for current-controlled PMSM drives," *IEEE Trans. Ind. Appl.,* vol. 50, no. 5, pp. 3365-3373, Sep./Oct., 2014.
[26] Y. Cho, T. LaBella and J. S. Lai, "A three-phase current reconstruction strategy with online current offset compensation using a single current sensor," *IEEE Trans. Ind. Electron.,* vol. 59, no. 7, pp. 2924-2933, Jul. 2012.
[27] D. W. Chung and S. K. Sul, "Analysis and compensation of current measurement error in vector-controlled AC motor drives," *IEEE Trans. Ind. Appl.,* vol. 34, no. 2, pp. 340-345, Mar./Apr., 1998.
[28] G. L. Wang, D. X. Xiao, G. Q. Zhang, C. R. Li, X. G. Zhang and D. G. Xu, "Sensorless control scheme of IPMSMs using HF orthogonal square-wave voltage injection into a stationary reference frame," *IEEE Trans. Power Electron.,* vol. 34, no. 3, pp. 2573-2584, Mar. 2019.
[29] Q. P. Tang, A. W. Shen, P. Luo, H. L. Shen, W. H. Li and X. N. He, "IPMSMs sensorless MTPA control based on virtual q-axis inductance by using virtual high frequency signal injection," *IEEE Trans. Ind. Electron.,* DOI: 10.1109/TIE.2018.2890487, 2019.
[30] Q. P. Tang, A. W. Shen, X. Luo and J. B. Xu, "IPMSM sensorless control by injecting bidirectional rotating HF carrier signals," *IEEE Trans. Power Electron.,* vol. 33, no. 12, pp. 10698-10707, Dec. 2018.
[31] G. L. Wang, D. X. Xiao, N. N. Zhao, X. G. Zhang, W. Wang and D. G. Xu, "Low-frequency pulse voltage injection scheme-based sensorless control of IPMSM drives for audible noise reduction," *IEEE Trans. Ind. Electron.,* vol. 64, no. 11, pp. 8415-8426, Nov. 2017.
[32] X. X. Zhou, X. Chen, C. Peng and Y. P. Zhou, "High performance nonsalient sensorless BLDC motor control strategy from standstill to high speed," *IEEE Transactions on Ind. Infor.*, vol. 14, no. 10, pp. 4365-4375, Oct. 2018.
[33] S. C. Yang and G. R. Chen, "High-speed position-sensorless drive of permanent-magnet machine using discrete-time EMF estimation," *IEEE Trans. Ind. Electron.,* vol. 64, no. 6, pp. 4444-4453, Nov. 2017.
[34] Y. R. Wang, Y. X. Xu and J. B. Zou, "Sliding mode sensorless control of PMSM with inverter nonlinearity compensation," *IEEE Trans. Power Electron.,* DOI: 10.1109/TPEL.2018.2890564, 2019.

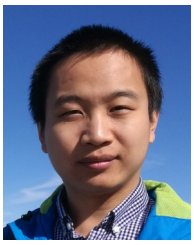

Jiadong Lu (M'19) was born in Pucheng, China, 1990. He received the B.S., the M.S. and the Ph.D. degrees in electrical engineering from Northwestern Polytechnical University (NWPU), Xi'an, China in 2012, 2015 and 2018, respectively. Between 2017 and 2018, he was with the Department of Electrical Engineering, Electronics and Computer Science, University of Liverpool (UoL), U.K. as an Honorary Academic Researcher. Currently, he is an Associate Research Fellow at the Department of Electrical Engineering, NWPU.

His research interests include hybrid-fault-tolerant control techniques for permanent magnet synchronous motor drives, aging issue for motor drives and power electronics converters & control.

Yihua Hu (M'13-SM'15) received the B.S. degree in electrical engineering in 2003, and the Ph.D. degree in power electronics and drives in 2011, both at China University of Mining and Technology. Between 2011 and 2013, he was with the College of Electrical Engineering, Zhejiang University as a Postdoctoral Fellow. Between 2013 and 2015, he worked as a Research Associate at the power electronics and motor drive group, the University of Strathclyde. Between 2016 and 2019, he was a Lecturer at the Department of Electrical Engineering and Electronics, University of Liverpool (UoL). Currently, he is a reader at Electronics Engineering Department at University of York (UoY). He has published 85 papers in IEEE Transactions journals. His research interests include renewable generation, power electronics converters & control, electric vehicle, more electric ship/aircraft, smart energy system and non-destructive test technology. He is the associate editor of IEEE Transactions on Industrial Electronics, IET Renewable Power Generation, IET Intelligent Transport Systems and Power Electronics and Drives.

Jinglin Liu (M'01) received the B.Eng. degree in electrical engineering from Tsinghua University, Beijing, China, in 1986, and the M.Eng. and the Ph.D. degrees in electrical engineering from NWPU, Xi'an, China, in 1990 and 2002, respectively. Since 1994, he has been a Faculty Member with NWPU, Xi'an, where he is currently a Professor of Electrical Engineering. His research interests include electrical machines design and drives, power electronics, fault diagnosis, and motion control.

Kai Ni (S'17) was born in Jiangsu, China. He received the B.Eng. (Hons) degrees in Electrical Engineering and Automation from Xi'an Jiaotong Liverpool University, Suzhou, China, and Electrical Engineering from the University of Liverpool, Liverpool, UK, in 2016. He is currently pursuing the Ph.D. degree at the University of Liverpool. His research interests include operation and control of doubly-fed induction machines, power electronic converters, and power systems.

Huiqing Wen (M'13-SM'18) received his B.S. and M.S. degrees in Electrical Engineering from Zhejiang University, Hangzhou, China, in 2002 and 2006; and his Ph.D. degree in Electrical Engineering from the Chinese Academy of Sciences, Beijing, China, in 2009. From 2009 to 2010, he was an Electrical Engineer working in the Research and Development Center, GE (China) Co., Ltd., Shanghai, China. He is presently working as an Associate Professor at the Xi'an Jiaotong-Liverpool University, Suzhou, China. His current research interests include power electronics and renewable energy.